18th Brazilian Congress of Thermal Sciences and Engineering
November 16–20, 2020 (Online)

ENC-2020-0175
STATISTICS OF TURBULENT FLOWS COMPUTED BY LARGE EDDY SIMULATIONS OF A NACA0012 AIRFOIL

Gabriel B. Nogueira
gabrielbarrosnog@gmail.com
Túlio R. Ricciardi
tulioricci@gmail.com
William R.Wolf
wolf@fem.unicamp.br
School of Mechanical Engineering, University of Campinas, 13083-860, Campinas - SP, Brazil

Abstract. *The study of turbulent flows over airfoil profiles finds application in aeronautical and wind energy research where drag and noise reduction are sought. In this work, we combine wall-resolved large eddy simulations with statistical post-processing tools to provide a better understanding of physical processes related to turbulent flows in the presence of walls with adverse pressure gradient variations. An investigation of the mechanisms of production, advection, diffusion, transport and dissipation is provided through analysis of turbulent kinetic energy (TKE) budgets. Turbulence anisotropy effects are studied using the scatter plots of velocity components and probability density functions. The impact of mesh refinement on the convergence of statistics is also verified. Moreover, different tripping configurations are analyzed to assess their impact on the boundary layers.*

Keywords: *Large eddy simulation, Turbulent flow, Aerodynamics, Anisotropy, Turbulent kinetic energy*

1. INTRODUCTION

Studies of flows past airfoil profiles find application in the design of aircraft wings, industrial rotors (Gourdain *et al.*, 2017), and wind and gas turbines for energy production (Li *et al.*, 2015; Oerlemans, 2009). More recently, airfoil flows have also been studied for the design of micro-air-vehicles (MAVs) (Truong *et al.*, 2013), where there is interest in mimicking both the flight and performance of birds and insects. Airfoil flows are also important for developing unmanned aerial vehicles (UAVs) with reduced drag and noise. In this context, a new class of vehicles including quadcopters and drones is attracting engineers and scientists to design shrouded rotors with more efficient airfoils with enhanced lift characteristics.

Most applications of the airfoil flows described above occur at sufficiently high Reynolds numbers for which the boundary layers and wakes are turbulent. In order to understand the characteristics of different airfoils for a range of applications, a study of turbulence properties for such flows is necessary. In this work, we employ high fidelity simulations, in particular, large eddy simulations (LES), of turbulent flows past a NACA0012 airfoil at 5 degrees angle of incidence. Although there are several studies of free shear flows and channels (Pope, 2000) in the literature, applications of wall-resolved LES to airfoils represent a more recent topic of study. Differently from channel flows, airfoils have finite chords and, hence, represent a combination of wall-bounded turbulent flows, i.e. , along the chord of the airfoil with free shear flows on wake of the airfoil. The effects of anisotropy found in channel flows are also present in this class of flows but, here, the pressure gradient has a variation. Airfoil flows may also be heavily tripped to mimic wind tunnel experiments, a condition that is not found in channel flows. Such tripping mechanism may introduce different turbulent structures in the flow which have important roles in noise generation and drag.

We present a study of turbulence quantities in flows over a NACA0012 airfoil trying to understand physical phenomena related to tripping and large-scale turbulent structures. LES of airfoil flows may add some non-physical characteristics to the flow such as periodical boundary conditions and filtering of small-scale structures. In this work, we will provide an assessment of such features. Different Reynolds numbers will be analyzed and an investigation of the mechanisms of production, advection, diffusion, transport and dissipation is provided through analysis of turbulent kinetic energy (TKE) budgets. Turbulence anisotropy effects are studied using scatter plots of velocities components and probability density functions. The impact of mesh refinement on the convergence of statistics is also verified.

2. NUMERICAL METHODOLOGY

The present LES calculations solve the compressible Navier Stokes equations in conservative form using general curvilinear coordinates. The equations are written in conservation form as

$$\frac{\partial \rho}{\partial t} + \frac{\partial (\rho u_i)}{\partial x_i} = 0 \, , \tag{1}$$

$$\frac{\partial (\rho u_i)}{\partial t} + \frac{\partial (\rho u_i u_j \; + g^{ij} p - \tau_{ij})}{\partial x_j} = 0 \, , \tag{2}$$

$$\frac{\partial E}{\partial t} + \frac{\partial \left[(E + p) \, u_j \; - \tau_{ij} g_{ik} u_k + q_j \, \right]}{\partial x_j} = 0 \, , \tag{3}$$

where u_i, ρ, and p are the contravariant velocity components, density, and pressure, respectively. The total energy E, the viscous stress tensor τ_{ij}, and the heat flux q_j for a fluid obeying Fourier's law are given by

$$E = \frac{p}{\gamma - 1} \; + \; \frac{1}{2} \rho g_{ik} u_i u_k \; , \tag{4}$$

$$\tau_{ij} = \frac{\mu}{Re} \left(g^{jk} \frac{\partial u_i}{\partial x_k} + g^{ik} \frac{\partial u_j}{\partial x_k} - \frac{2}{3} g^{ij} \frac{\partial u_k}{\partial x_k} \right) \; , \tag{5}$$

and

$$q_j = - \frac{\mu}{RePr} \, g^{ij} \frac{\partial T}{\partial x_i} \; . \tag{6}$$

Assuming the medium to be a calorically perfect gas, the set of equations is closed by the equation of state

$$p = \frac{\gamma - 1}{\gamma} \rho T \; . \tag{7}$$

In the previous equations, g_{ij} and g^{ij} are the covariant and contravariant metric tensors, respectively. The equations are solved in nondimensional form where length, velocity components, density, pressure, and temperature are nondimensionalized by a reference length C, freestream speed of sound c_∞, freestream density ρ_∞, $\rho_\infty c_\infty^2$, and $(\gamma - 1) T_\infty$, respectively. Here, T is the temperature; γ is the ratio of specific heats; Re is the Reynolds number, defined as $Re = Re_a M_\infty$, where $Re_a = \rho_\infty c_\infty C / \mu_\infty$ and $M_\infty = U_\infty / c_\infty$; Pr is the Prandtl number, defined as $Pr = \mu_\infty c_p / \kappa_\infty$; c_p is the heat capacity at constant pressure; μ is the viscosity coefficient and κ is the thermal conductivity coefficient.

The spatial discretization of the equations is performed using a compact scheme of sixth order accuracy (Nagarajan *et al.*, 2003) implemented in a staggered mesh. This finite difference schemes are non-dissipative and, consequently, there is a need for filtering the solution, once numerical instabilities may grow due to non-uniform meshes and other numerical discretization errors. The filter is applied only at high wavelengths in order to preserve the physics of turbulence (Lele, 1992). In the present simulations, we make use of overset grids with a fourth-order accurate Hermite interpolation between grid blocks (Bhaskaran *et al.*, 2010) in order to better resolve the boundary layers and wakes along the airfoil.

The temporal integration of the equations are carried out by a second-order scheme of (Beam and Warming, 1978) in the near-wall region in order to overcome the time step restriction typical of very fine wall-normal boundary layer grids. Away from solid walls, we advance the solution over time using a compact storage third-order Runge-Kutta scheme. In the wall boundaries, the non-slip condition is employed for an adiabatic wall. In the spanwise direction we employ a periodic boundary condition and, in the farfield, boundary conditions are based on characteristic variables (Riemann invariants), besides the application of a buffer layer which dissipates acoustic waves (Wolf, 2011). Different simulations are performed in this work and we assess the effects of a dynamic Smagorinsky (Lilly, 1992) subgrid model on the solutions. In this sense, the SGS model is switched on and off, depending on the simulation and, therefore, the simulations become implicit LES (ILES).

3. FLOW AND MESH CONFIGURATIONS

All simulations studied in this work are run for a flow configuration with Reynolds number based on the airfoil chord $Re_c = 408.000$ and freestream Mach number $M_\infty = 0.115$. The airfoil is set at 5 degrees angle of attack with the incoming flow laminar. Results are compared to previous studies by (Wolf, 2011). The present mesh configurations consist of body-fitted O-grid blocks designed to accurately resolve the turbulent boundary layer on the suction side of the airfoil. The O-grid blocks have a greater concentration of points (approximately 75%) in the suction side and use a mesh stretching consisting of a hyperbolic tangent function in the wall-normal direction. In the background, a Cartesian grid block with uniform resolution around the O-grid block is employed using an overset mesh procedure. Figure 1 shows a comparison of the meshes used in the investigation. A detail view of the O-grid can be also seen. In Fig. 1 (d), one may notice the vertical divisions in the O-mesh. These are due to the output in CGNS format which facilitates the mesh visualization and post-processing in zones. The figures show every 6 points in order to allow a better visualization of the meshes.

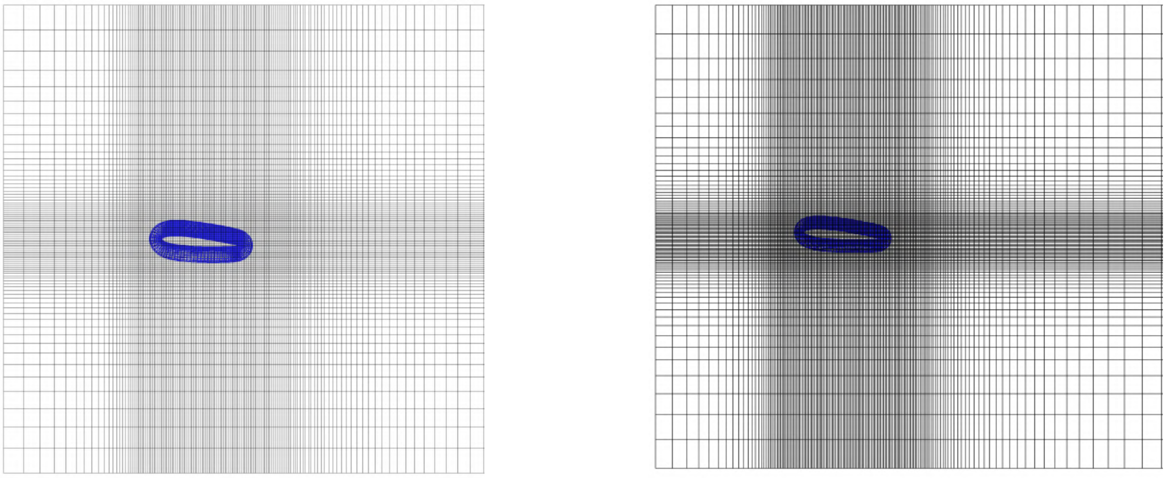

(a) Full view of the computacional grid used by (Wolf, 2011)

(b) Full view of refined computacional grid

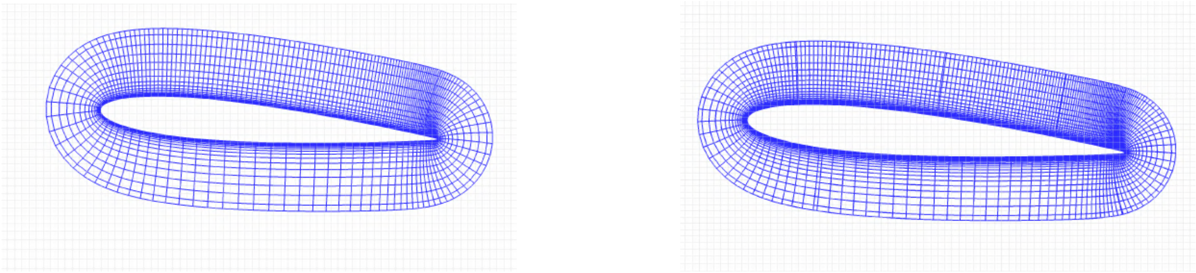

(c) Detail view of O-grid by (Wolf, 2011)

(d) Detail view of refined O-grid

Figure 1. Comparison of different grids for NACA0012 airfoil (every 6th grid point shown).

The results of the simulation conducted are presented in Fig. 2 in terms of iso-surfaces of Q-criterion. It is possible to observe the development of the turbulent boundary layer along the suction side of the airfoil. For this case, the tripping is two-dimensional and some 2D structures form downstream the tripping region. Later, these structures are disturbed transitioning to a fully turbulent flow as can be seen in the detail view of the trailing edge region.

3.1 TRIPPING CONFIGURATION

Different tripping configurations are tested in order to disturb the boundary layer. Two-dimensional and three-dimensional steady tripping are employed in regions with suction along $0.15 < x/c < 0.175$ and blowing over the region $0.175 < x/c < 0.20$. The suction and blowing have magnitudes $U_{blowing} = -U_{suction} = 0.03\ U_\infty$, where U_∞ represents the freestream velocity. Due to tripping and an adverse pressure gradient, the boundary layer becomes turbulent on the suction side of the airfoil. On the pressure side, the boundary layer remains laminar since no tripping is applied in this region and the flow has a favorable pressure gradient.

Wolf (Wolf, 2011) employed a three-dimensional tripping (3D) in the spanwise direction where the dimension along the span z/s of tripping is $10\% < z/s < 90\%$. However, we also tested a two-dimensional tripping (2D) as discussed in (Ricciardi *et al.*, 2019). When the 2D tripping is applied, the SGS subgrid model is switched off while the 3D tripping has the SGS model turned on. In order to identify possible "artificial" non-physical structures caused by the previous tripping configurations (3D and 2D), a random tripping has been implemented with variations in space and time.The function that determines the distribution of random tripping along the span is composed by a harmonic function, where wavenumbers

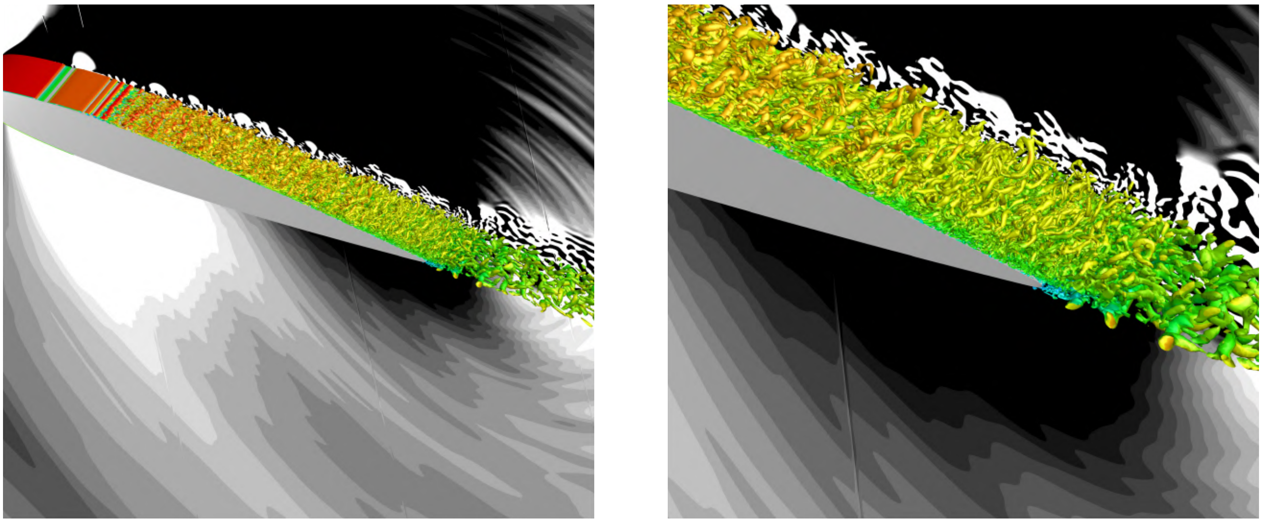

(a) Isosurfaces of Q criterion

(b) Detail view of the flow along the trailing edge

Figure 2. Iso-surfaces of Q criterion for the flow configuration with 2D tripping.

are excited until Nyquist's frequency.

$$S(z) = \sum_{k=1}^{Nz/2} Amp\ sin(kz+\phi) \quad , \quad U_{jet} = 0.03\, U_{\infty} \quad , \quad U = U_{jet}\ rand(Amp) \tag{8}$$

A random amplitude modulates the velocity of the tripping region and a Gaussian distribution is used to smooth out the disturbance along the flow direction along the tripping region. The tripping is modified temporally and different settings of tripping are shown in Fig. 3. Table 1 presents details between meshes in terms of resolution and tripping configuration.

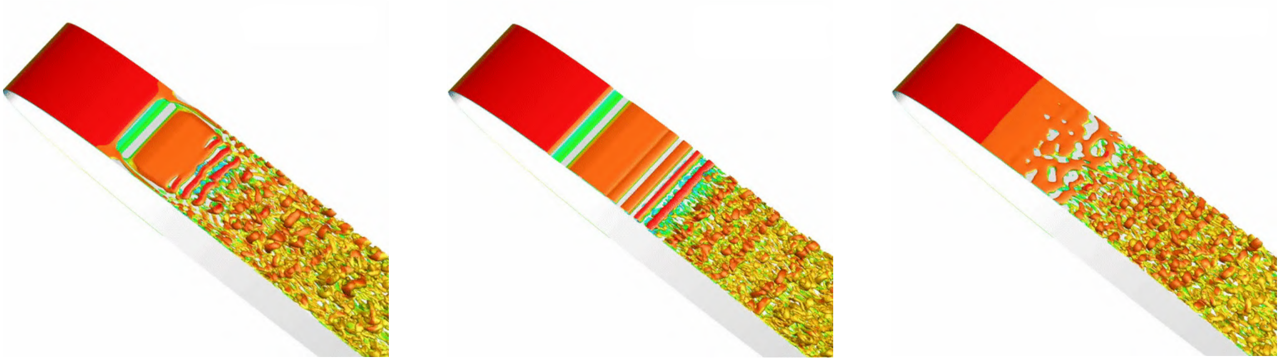

(a) 3D tripping

(b) 2D tripping

(c) Random tripping

Figure 3. Comparison of different tripping configurations.

Table 1. Different meshes and tripping configurations. The values n_x,n_y,n_z represent the number of points in the x, y, z coordinates, respectively. The terms Δx^+_w, Δy^+_w and Δz^+_w depict the mesh resolution on the first element near the airfoil surface, in viscous units. The subscripts "max" and "TE" represent maximum values computed along the airfoil surface and those near the airfoil trailing edge, along the suction side.

Simulations	*O-grid* (n_x,n_y,n_z)	$\Delta x^+_{w_{max}}$	$\Delta y^+_{w_{max}}$	$\Delta z^+_{w_{max}}$	$\Delta x^+_{w_{TE}}$	$\Delta y^+_{w_{TE}}$	$\Delta z^+_{w_{TE}}$	*Tripping*
1	960 x 125 x 128	63.5	0.63	21	14.5	0.39	13	3D
2	1200 x 190 x 144	50.5	0.58	18	11	0.37	11.5	2D
3	960 x 125 x 128	63.5	0.63	21	14.5	0.39	13	Random

3.2 COEFFICIENTS OF FRICTION C_f AND PRESSURE C_p

Figure 4 (a) shows the surface distribution of friction coefficient defined as $C_f = \frac{\tau_w}{(1/2\rho U_e)}$. Here, τ_w is the wall shear stress and U_e is the velocity at the edge of the boundary layer. As can be seen, all simulations present good agreement.

However, for the 2D tripping, there is a region of negative friction coefficient which indicates the appearance of a small recirculation bubble just downstream the blowing region. The 3D tripping keeps the flow absent from this bubble probably because of longitudinal vortical structures that add momentum to the flow. The random tripping provides the best result in terms of friction coefficient as it is the smoothest curve. Figure 4 (b) shows the distribution of pressure coefficient C_p along the airfoil surface. Results are compared to the simulation by (Wolf, 2011), an Xfoil code solution(Drela, 1989) and potential flow theory. As can be noticed, there is a good agreement among all results. Xfoil captures a stronger suction peak at the leading edge but, overall, solutions are similar. Similarly to the friction coefficient, for the random tripping the pressure coefficient is also smoothed out along the tripping region. The potential flow solution has a small discrepancy at the trailing edge due to its non-viscous nature.

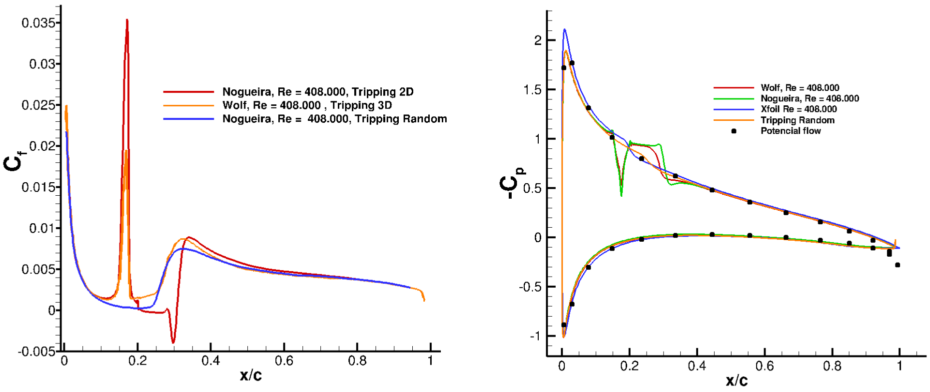

(a) Distribution of C_f along the airfoil chord (b) Distribution of $-C_p$ along the airfoil chord

Figure 4. Distribution of C_f along the airfoil chord (a) and $-C_p$ along the airfoil chord (b).

3.3 MEAN VELOCITY AND REYNOLDS STRESS PROFILES

Figure 5 shows the mean velocity profiles normalized by friction velocity as function of wall units y^+. As in (Wolf, 2011), the log law regions presents a shift in the mean velocity profile when compared to the standard log-law. In the same figure, one can see the mean velocity profiles of (Ricciardi *et al.*, 2019) obtained with the two-dimensional tripping in the suction side and for the random tripping. Results demonstrate that the tripping configurations do not have a considerable impact on the mean velocity profiles. A mesh refinement is employed and causes a small change in the slope of the log region when compared to the typical von Kármán slope obtained for a flat plate.

Although the mean velocity profiles do not match the classical log-law for flat plates, we show that the results match with experiments using TOMO-PIV performed for NACA0012 airfoils at similar flow conditions (Ghaemi and Scarano, 2011). Therefore, possible variations of pressure gradient on the airfoil, as well as curvature and Reynolds number effects, may shift the velocity profiles for the airfoil flows compared to the classic flat plate.

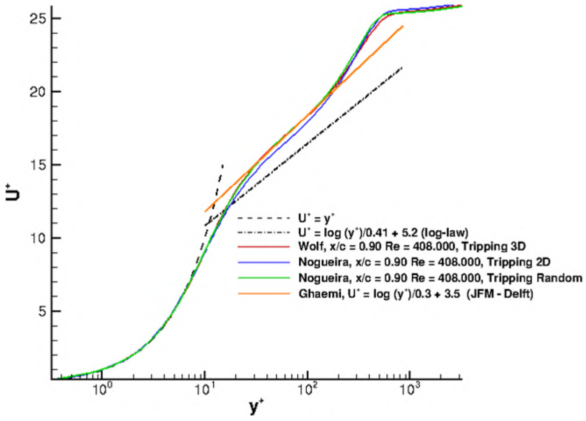

Figure 5. Mean velocity profiles normalized by friction velocity.

Some further flow statistics are shown in Fig. 6 through the distribution of Reynolds stresses normalized by friction velocity for different tripping configurations at the position x/c = 0.90 of the airfoil. As one can see, results obtained for the 2D, 3D (Wolf, 2011) and random tripping are similar. However, note that for the Reynolds tensor component $\langle u_1 u_1 \rangle$

the maximum value for 3D tripping and random tripping have the same magnitude, while 2D tripping has a smaller magnitude.

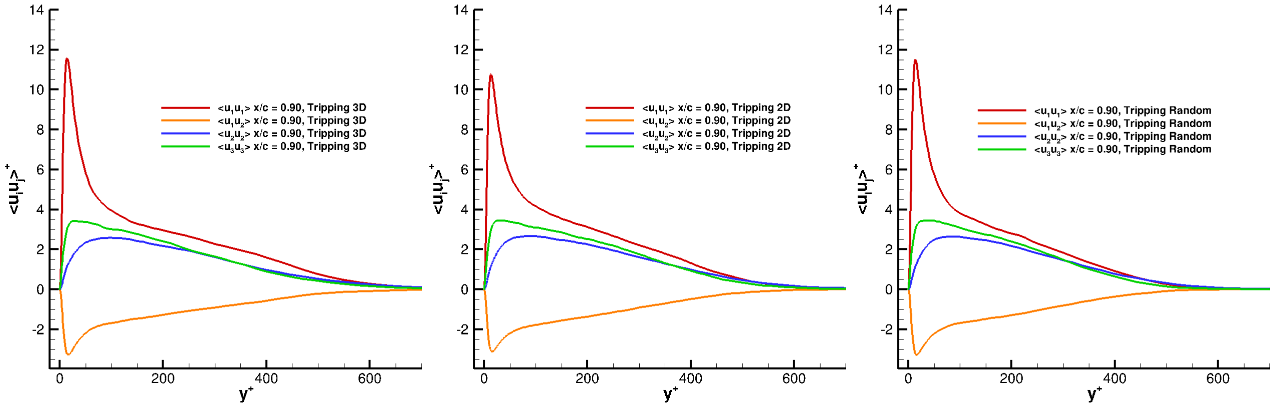

(a) Tripping 3D (b) Tripping 2D (c) Tripping random

Figure 6. Reynolds stresses normalized by friction velocity.

3.4 TURBULENT KINETIC ENERGY BUDGET

Turbulent kinetic energy (TKE) budgets are computed along the chord to ascertain the effects of adverse pressure gradient on production, dissipation and diffusion of turbulence. The turbulent kinetic energy transport equation can be written as:

$$\frac{\partial k}{\partial t} = A + P + T + D + D_p - \epsilon \,. \tag{9}$$

This equation indicates the balance of advection, production, turbulent transport, viscous diffusion, pressure diffusion, and pseudo-dissipation for turbulent kinetic energy. For a statistically stationary flow, the time derivative must be zero. The terms in the right-hand side of the previous equation are defined as:

$$\text{Advection:}\;\; A = -\left\langle U_j \right\rangle \frac{\partial k}{\partial x_j} \,, \tag{10}$$

$$\text{Production:}\;\; P = -\left\langle u_i^{'} u_j^{'} \right\rangle \frac{\langle \partial U_i \rangle}{\partial x_j} \,, \tag{11}$$

$$\text{Turbulent transport:}\;\; T = -\,\frac{1}{2} \frac{\partial \left\langle u_i^{'} u_i^{'} u_j^{'} \right\rangle}{\partial x_j} \,, \tag{12}$$

$$\text{Viscous diffusion:}\;\; D = \nu \,\frac{\partial^2 k}{\partial x_j^2} \,, \tag{13}$$

$$\text{Pressure diffusion:}\;\; D_p = -\frac{1}{\rho} \frac{\partial \left\langle u_i p^{'} \right\rangle}{\partial x_i} \,, \tag{14}$$

$$\text{Pseudo-dissipation:}\;\; \epsilon = -\nu \left\langle \frac{\partial u_i}{\partial x_j} \frac{\partial u_i}{\partial x_j} \right\rangle \,. \tag{15}$$

All derivatives are calculated using a 10th order compact scheme along with the respective metric terms for the derivatives along the x and y directions.Results are shown for different trippings of the airfoil in Fig. 7 .

The TKE budgets are made non-dimensional by the factor of $\frac{u_\tau^4}{\nu}$ (Pope, 2000). It is first noticed that very close to the wall, the kinetic energy balance is zero. Note also that for $y^+ \approx 10$ there is the highest level of turbulence production. At $y^+ \approx 20$ there is the largest error in the TKE balance and this difference is attributed to the filtered scales in the LES which are not present in the pseudo-dissipation term. The behavior of TKE for the 3D, 2D, and random tripping are very similar, with a significant increase mainly in the terms of the turbulent diffusion and viscous diffusion in the 3D and random tripping.

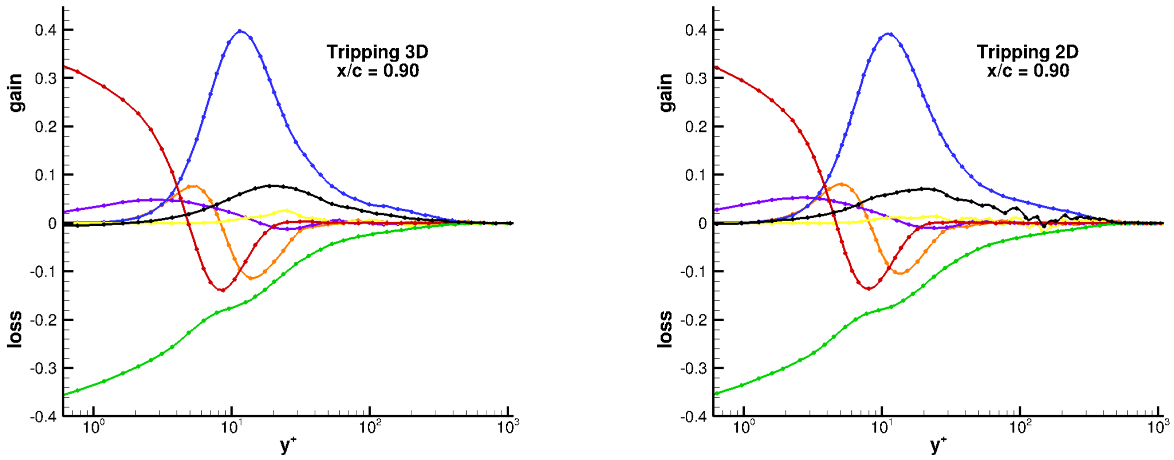

(a) 3D tripping

(b) 2D tripping

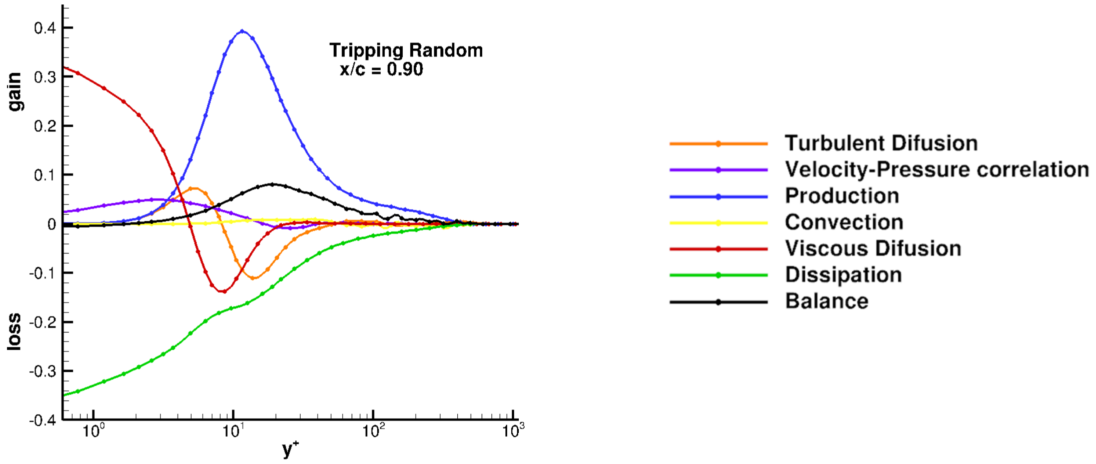

(c) Random tripping

Figure 7. TKE budgets for different tripping configurations at x/c = 0.90.

3.5 PROBABILITY DENSITY FUNCTIONS

Studies of coherent structures in turbulence have always called the attention of researchers. In wall-bounded turbulence, streaks and hairpins are frequently analyzed. The physical mechanism of formation of the latter is due to velocity fluctuations in the wall-normal and tangential components along the boundary layer. The previous coherent structures are directly affected by sweeps and ejections that occur in the boundary layer induced by outboard and inboard flows. Such observations are evidenced in the following scatter plots of velocities fluctuations.

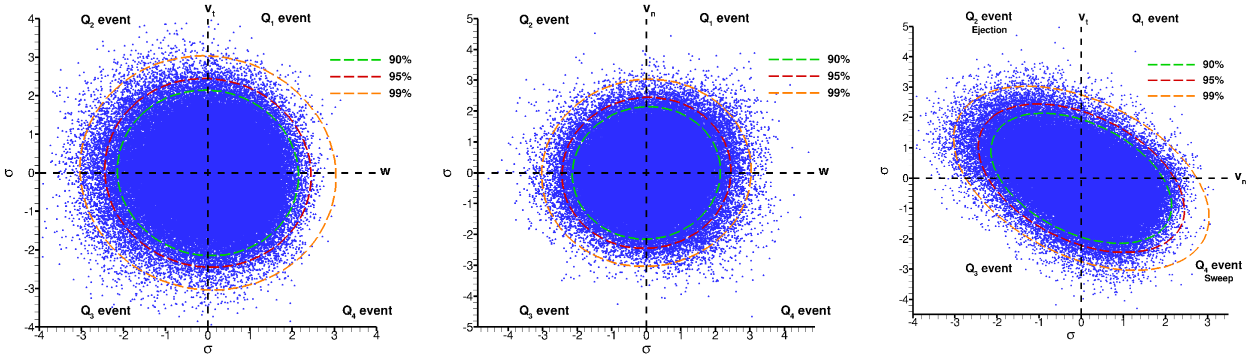

(a) Scatter - $v_t w$ (b) Scatter - $v_n w$ (c) Scatter - $v_t v_n$

Figure 8. Distribution of velocities normalized by standard deviation at x/c = 0.70 and $y^+ = 50$

In the scatter plots, data is normalized by the respective standard deviation and the curves are obtained for the random tripping configurations. However, all tripping methodologies tested exhibited the same behavior. Here, we show results for $x/c = 0.70$ and $y^+ = 50$. Covariance error ellipses are also shown for 90%, 95% and 99% values. The distributions of velocity fluctuations uw and vw are circular and uniform unlike uv, which has a preferred direction typical of the principal Reynolds shear stresses. One can see from the plots that sweeps and ejections occur for the Q_4 and Q_2 quadrants, respectively, with more extreme values of ejections at $y^+ = 50$.

The same physical mechanism of ejections and sweeps is also evident when computing probability density functions (PDFs). Here, the PDFs are obtained for the random tripping at x/c = 0.70 for $y^+ = 5$, 10, 15,20,50 and 100. All PDFs are normalized by their respective standard deviations. A kernel distribution is used to provide a nonparametric representation of the PDF. The PDF is written as a function of the kernel as

$$f_h(V) = \frac{1}{nh} \sum_{i=1}^{n} K\left(\frac{v - v_i}{h}\right) \tag{16}$$

where $v_1, v_2, \ldots, v_n$ are random samples from an unknown distribution, n is the sample size, K(·) is the kernel smoothing function, and h is the bandwidth.

The distributions for velocity fluctuations v_t, v_n and w are shown respectively in Fig. 9 together with the respective skewness μ_3 and kurtosis μ_4 values shown in the tables 2, 3 and 4 .

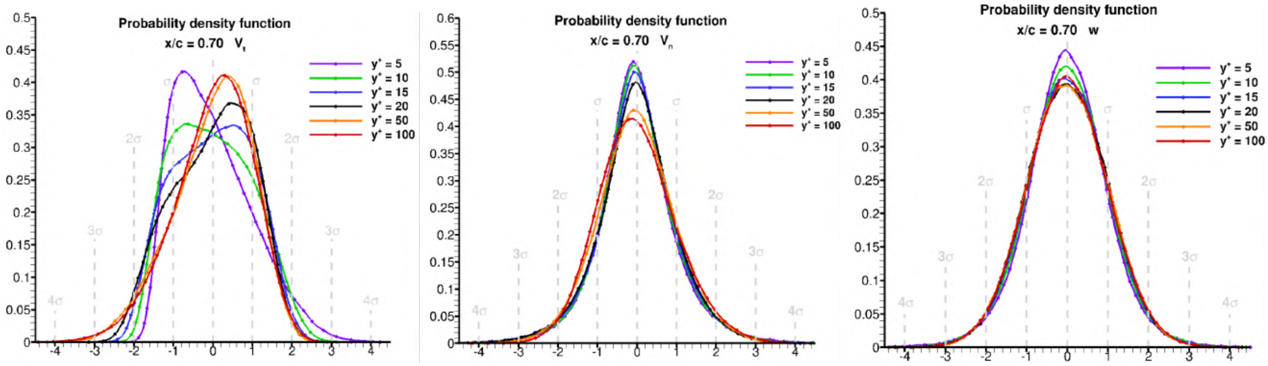

(a) Probabilitity density function for v_t.
(b) Probabilitity density function for v_n.
(c) Probabilitity density function for w.

Figure 9. Probabilitity density function for v_t,v_n and w.

Table 2. Skewness μ_3 and Kurtosis μ_4 for v_t.

$\mu_3^{y^+=5}$	0.686	$\mu_4^{y^+=5}$	3.034
$\mu_3^{y^+=10}$	0.226	$\mu_4^{y^+=10}$	2.231
$\mu_3^{y^+=15}$	-0.044	$\mu_4^{y^+=15}$	2.146
$\mu_3^{y^+=20}$	-0.233	$\mu_4^{y^+=20}$	2.271
$\mu_3^{y^+=50}$	-0.475	$\mu_4^{y^+=50}$	2.912
$\mu_3^{y^+=100}$	-0.481	$\mu_4^{y^+=100}$	3.192

Table 3. Skewness and Kurtosis for v_n.

$\mu_3^{y^+=5}$	0.165	$\mu_4^{y^+=5}$	5.714
$\mu_3^{y^+=10}$	0.001	$\mu_4^{y^+=10}$	5.119
$\mu_3^{y^+=15}$	-0.093	$\mu_4^{y^+=15}$	4.664
$\mu_3^{y^+=20}$	-0.127	$\mu_4^{y^+=20}$	4.197
$\mu_3^{y^+=50}$	0.073	$\mu_4^{y^+=50}$	3.300
$\mu_3^{y^+=100}$	0.281	$\mu_4^{y^+=100}$	3.245

The results for the PDFs are compared with (Wacławczyk *et al.*, 2004) and (Dinavahi, 1992), which present results obtained for a turbulent channel flow and they exhibit excellent agreement. For the tangential velocity v_t we note the

Table 4. Skewness and Kurtosis for w.

$\mu_3^{y^+=\,5}$	-0.055	$\mu_4^{y^+=\,5}$	4.314
$\mu_3^{y^+=\,10}$	-0.022	$\mu_4^{y^+=\,10}$	3.616
$\mu_3^{y^+=\,15}$	-0.008	$\mu_4^{y^+=\,15}$	3.284
$\mu_3^{y^+=\,20}$	-0.004	$\mu_4^{y^+=\,20}$	3.086
$\mu_3^{y^+=\,50}$	-0.014	$\mu_4^{y^+=\,50}$	2.985
$\mu_3^{y^+=\,100}$	0.007	$\mu_4^{y^+=\,100}$	3.066

change in positive skewness (associated with ejections) to a negative skewness (associated with sweeps) along the boundary layer. This mechanism also occurs for the normal velocity v_n, however, it is more subtle for skewness. On the other hand, kurtosis will change with increasing y^+, approaching the typical value of 3 for a Gaussian distribution. As expected, the PDF of w velocity component is a Gaussian distribution as can be also inferred from its skewness and kurtosis.

4. CONCLUSIONS

In the current work we employ wall-resolved large eddy simulations to study turbulent flows over a NACA 0012 airfoil. Statistics of the turbulent flows are analyzed in terms of TKE budgets and PDFs. We also show comparisons in terms of pressure and friction coefficients, as well as mean velocity and Reynolds stress profiles. Results show agreement for all different tripping and mesh configurations with some subtle changes in some of the statistics.

Statistics obtained by the 3D, 2D and random trippings are similar for the current analyses despite that, for the 2D tripping configuration, a small separation bubble is observed just downstream of the tripping location. On the other hand, for the 3D tripping, the flow is fully attached, probably because of longitudinal vortices from the tripping that add streamwise momentum to the flow. The random tripping is more recommended to disturb the boundary layer as showed on C_f and C_p distributions. However, it is not recommended for acoustic analysis due to its inherent noise generation. The physical mechanism of ejections and sweeps is evidenced in both scatter plots and PDFs.

5. REFERENCES

Beam, R. and Warming, R., 1978. "An implicit factored scheme for the compressible navier-stokes equations". *AIAA Journal,*, Vol. 16, pp. 393–402.

Bhaskaran, R. and S.K., L., 2010. "Large eddy simulation of free-stream turbulence effects on heat transfer to a high pressure turbine cascade". *Journal of Turbulence,*, Vol. 11, No. 1, pp. 1–15.

Dinavahi, S.P.G., 1992. "Probability density functions in turbulent channel flow". *Tech. rep., NASA Reference Publication*.

Drela, M., 1989. "XFOIL: An analysis and design system for low reynolds number airfoils". *Conference Notre Dame, Indiana, USA*, Vol. 54.

Ghaemi, S. and Scarano, F., 2011. "Counter-hairpin vortices in the turbulent wake of a sharp trailing edge". *Journal of Fluid Mechanics*, Vol. 689, p. 317–356.

Gourdain, N., Singh, D., Jardin, T. and S.Prothin, 2017. "Analysis of the turbulent wake generated by a micro air vehicle hovering near the ground with a lattice boltzmann method". *Journal of the american helicopter society*, Vol. 62, pp. 1–12.

Lele, S., 1992. "Compact finite difference schemes with spectral-like resolution". *Journal of Computational Physics,*, Vol. 103, pp. 16–42.

Li, Y., Castro, A., Sinokrot, T. and Carrica, W.P.P., 2015. "Coupled multi-body dynamics and cfd for wind turbine simulation including explicit wind turbulence". *Elsevier*, Vol. 76, pp. 338–361.

Lilly, D.K., 1992. "A proposed modification of the germano subgridscale closure method". *Physics of Fluids A: Fluid Dynamics*, Vol. 4, pp. 633–635.

Nagarajan, Lele, S., S.K. and Ferziger, J., 2003. "A robust high-order method for large eddy simulation". *Journal of Computational Physics,*, Vol. 191, p. 392–419.

Oerlemans, S., 2009. *Detection of aeroacoustic sound sources on aircraft and wind turbines*. Ph.D. thesis, University of Twente.

Pope, S.B., 2000. *Turbulent Flows*. Cambridge University Press, New York, 1st edition.

Ricciardi, T.R., Ribeiro, J.H.M. and Wolf, W.R., 2019. "Analysis of coherent structures in large-eddy simulations of a NACA0012 airfoil". *AIAA Scitech 2019 Forum*.

Truong, T.V., Byun, D., Kim, M.J., Yoon, K. and C.Park, H., 2013. "Aerodynamic forces and flow structures of the leading edge vortex on a flapping wing considering ground effect". *IOP Science Journals*, Vol. 8.

Wacławczyk, M., Pozorski, J. and Minier, J., 2004. "Probability density function computation of turbulent flows with a new near-wall model". *Physics of Fluids*, Vol. 16.

Wolf, W.R., 2011. *Airfoil aeroacoustics: LES and acoustic analogy predictions*. Ph.D. thesis, Stanford University.

6. RESPONSIBILITY NOTICE

The authors are the only responsible for the printed material included in this paper.